Application of Miniature Sensors in the Development of Micro-climate Stations for Urban Climate Studies in Hong Kong

CHAN Kai-wing[1], CHAN Ying-wa[1], LAU Po-wing[1], NG Wai-wang[2] and Fan Man-hei[3]

[1]Hong Kong Observatory [2]Survey and Mapping Office, Lands Department
[3]Chinese University of Hong Kong
Correspondence: 134A Nathan Road, Tsim Sha Tsui, Kowloon, Hong Kong, China
Tel:+852 2926 8342, Fax: +852 2311 9448, Email: jkwchan@hko.gov.hk

Abstract

In 2017, the Hong Kong Observatory (HKO) implemented a pilot project and began operating 30-odd miniature passive (so called i-button) temperature sensors over the Kowloon peninsula at the city centre of Hong Kong. The main objective of the project is to study the temperature variations on a microscale under various meteorological scenarios with a view to better understanding the urban climate of Hong Kong. Initial analysis of the data highlighted wind corridors and significant heat sources that were influenced by urban developments, street orientations, geographical surroundings as well as human activities.

High resolution aerial thermal imageries over the area were also taken as a remote sensing technique for detailed diagnosis of the daytime and nighttime heat distribution over the Kowloon peninsula. Surface temperatures derived from the emissivity of the thermal imagery were compared with measurements made by i-button sensors installed on different land surfaces.

To further enhance the study with real-time data as well as inclusion of additional elements, such as relative humidity and wind, work is underway to develop and implement small package devices, such as microelectromechanical systems (MEMS) sensors, as well as IoT data transmission pathway say LoRaWAN for real-time monitoring. Moreover, application of 3-D printing technology has also opened the capability of development and fabrication of accessories for the micro-climate stations.

This paper presents the results obtained from the passive temperature sensors so far as well as highlights the steps in developing a network of micro-climate stations providing real-time weather data for use in urban climate studies and potential applications for smart city planning.

1. Introduction

The emergence of new miniature weather sensors and the advance of wireless communication technology provide great opportunities for the study of micro-climate in an urban environment where weather conditions can change rapidly in both temporal and spatial scales. To enhance understanding of the urban climate of Hong Kong, a metropolitan city at the southern coast of China, HKO established a dense network of micro-climate stations using a passive (so called i-button) temperature sensors in 2017. The network comprises more than 30 stations covering an area of around 4km x 4 km over the Kowloon peninsula at the centre of Hong Kong (Figure 1). The stations were set up in green parks, seaside areas, hilltops, roadsides, buildings, etc. so that a diversity of site environment can be achieved to study the different degrees of urban influences on temperature measurements. Details of the methodology including site selection, i-button sensor accuracy and characteristics, equipment setup, measurement results of Sky View Factor (SVF) at individual site and preliminary temperature observations in 2017 was summarized in Chan and Fan (2017).

In the second phase of the study, HKO liaised with the Lands Department of Hong Kong (LandsD) to take high-resolution aerial thermal photos covering the Kowloon peninsula so that surface temperatures of different surfaces derived from the emissivity values of the thermal photos could be compared with in-situ measurements made by i-button sensors placed on the surfaces. Also, the micro-climate station network has been further enhanced by installing MEMS sensors to allow measurements of additional elements such as relative humidity, air pressure and also wind speed and direction from a compact ultrasonic anemometer. IoT data transmission pathway using LoRaWAN has also been gradually implemented to facilitate real-time dissemination of weather data recorded by the micro-climate station network for prompt monitoring and analysis.

2. I-button temperature measurements in 2018

The first phase of the study by Chan and Fan (2017) showed that temperature distribution over the Kowloon peninsula was quite the opposite under easterly and westerly wind conditions. Under easterlies, temperatures over the eastern flank of the peninsula were lower due to lack of apparent heat sources upstream and probably better ventilation while higher temperatures were recorded downstream. Under westerlies, the temperature distribution pattern was essentially reversed. The results were likely related to the east-west orientated wind corridor that affected the ventilation conditions over the Kowloon peninsula and it was attributed to the natural topography and urban morphology in Hong Kong (Peng et

al., 2017). It was also found that traffic flow might influence the amount of artificial heat from vehicles released to the surrounding which was an important factor contributing to the relatively higher temperatures observed at roadside stations.

2.1 Easterly and westerly wind regimes

The very different temperature distribution over the Kowloon peninsula under easterly and westerly wind regimes was repeatedly observed during the prolonged hot spell that affected Hong Kong in May 2018. From 17 May to 1 June 2018, HKO issued the Very Hot Weather Warning (VHWW) which lasted for around 350 hours, a record since the introduction of the warning in 2000. The maximum temperature recorded by platinum resistance thermometer (PRT) at the HKO headquarters (HKOHq) rose above 33 degrees for a consecutive 16 days from 17 May to 1 June 2018 (HKO, 2018).

During the above 16-day heat wave period, there was a change of wind direction over the Kowloon peninsula from 31 May to 1 June 2018 with light to moderate west to southwesterlies prevailing on 31 May 2018 (Figure 2) but turning to generally easterlies the next day (Figure 3). Figures 4 and 5 show the temperature distribution over the Kowloon peninsula in these two days. On 31 May 2018, temperatures over the western flank of Kowloon peninsula near the seaside were in the region of 34-35°C while that over the eastern flank near the seaside were slightly higher (35-37°C). On the next day, temperatures over the eastern flank of Kowloon peninsula near the seaside were around 32-33°C, lower than those over the western flank near the seaside by 2 to 3°C. It was interesting to note that temperatures at HKO and A3 stations were susceptible to higher temperatures under easterlies. It was thought that the buildings to the east of HKO might cause blocking or introduce artificial heat sources that gave rise to such observation (Chan and Fan, 2017).

A comparison of the time series of temperatures recorded at T29, A3, HKO, T3 and T4 stations during the above 2-day period was conducted. These five stations are chosen with T29, A3 and HKO representing stations influenced more by winds from the west while T3 and T4 more by easterlies. As shown in Figure 6, temperatures at T29, A3 and HKO were generally lower on 31 May 2018 than those on 1 June 2018 while it was the reversed trend for temperatures at T3 and T4. These observations suggested that the former 3 stations would have better ventilation or less potential heat sources upstream when winds were generally from the west over the Kowloon peninsula. The same reason could be applied for the latter 2 stations when easterlies prevailed over the Kowloon peninsula. Although HKO was located more to the east geographically, it seemed to have better ventilation under the

westerly wind regime.

3. Remote sensing techniques for urban micro-climate studies

Applications of remote sensing techniques are presently more readily available for urban climate studies. The advantage of such approach is that it can provide a large spatial coverage for assessing the areal extent and characteristics of urban heat island. Previous research such as Huang et al. (2017) and Kaplan et al. (2018) made use of satellite imageries to study the spatiotemporal characteristics of urban heat island. However, due to limited resolution of satellite imageries, the fine details of heat distribution over the urban environment could hardly be revealed for in-depth analysis.

The present study utilizes thermal camera with a spectrum range of 7.5-14.0 μm wavelength to take high resolution (less than 1m) aerial thermal photos for urban micro-climate studies. The camera was operated by a trained officer from LandsD on a helicopter of the Government Flying Service of Hong Kong, cruising at an altitude ranging from around 600m to 700m and surveying the Kowloon peninsula during both daytime and nighttime periods. This was carried out on 14 January 2018 when the weather was generally fine that day which minimized the influence of low-level clouds on the quality of the thermal photos.

3.1 Surface temperatures derived from thermal photos

A thermal camera derives the temperature of an object by measuring its emitted infrared radiation, which does not only depend on the temperature of the object but is also a function of surface emissivity (Ɛ). The emissivity of a surface refers to its effectiveness in emitting infrared radiation and it depends on the material, nature of the surface and the surface's temperature. Emissivity ranges from 0 (shiny mirror) to 1 (blackbody). A clean and polished metal surface will have low emissivity whereas a roughened metal surface will have high emissivity. By knowing the characteristics of a surface, the atmospheric conditions at the time of taking thermal photos and the amount of infrared energy originated from the surroundings, one can estimate the temperature of the surface from the measured infrared radiation.

Thermal photos taken by the thermal camera on 14 January 2018 were used to derive the surface temperatures of different land surfaces at a few sites over the Kowloon peninsula. The derivation was performed by using a built-in algorithm of the camera with a number of parameters including emissivity, reflected apparent temperature, distance between the object

and the camera, mean temperature and mean relative humidity of the atmospheric column between the ground and the helicopter flight level. Two emissivity values were assigned to different materials for the temperature derivation, including Ɛ=0.95 for urban features and Ɛ=0.98 for vegetation and water features.

3.2 Generation of high resolution aerial thermal imagery

An ortho-rectified image removes geometric distortions inherent in the raw remotely-sensed photos such that the scale of the image is uniform and used in the same manner as a map. The generation of ortho-rectified thermal maps enables assessment of different characteristics of land surfaces which affect the heat balance of the urban environment. Significant heat sources contributing to urban heat island can also be identified.

As described in Section 3.1, pixels were classified into two emissivity classes based on conventional land cover classification approach using 4-channel (RGB and Near-infrared) orthophoto of LandsD and the ortho-rectified thermal maps. Figures 7 and 8 show the ortho-rectified thermal maps for the daytime and nighttime flights on 14 January 2018 respectively. The maps have a horizontal resolution of about 0.8m. Broadly speaking, blue areas are relatively cooler regions associated with trees and parks while red areas are hotter regions such as hot rooftops. For the daytime thermal map, some “hot spots” associated with artificial turf used in football pitch can be identified. For the nighttime thermal map, traffic and concrete roads are apparent heat sources. It is also interesting to note that the “hot spots” in daytime mostly had relatively lower temperatures at nighttime, indicating larger diurnal variation.

The surface temperatures derived were used to compare with measurements of i-button sensors placed on the surfaces. The comparison results for the daytime and nighttime flights on 14 January 2018 are shown in Table 1. Taking into account the limitations of emissivity-derived surface temperatures including the compensation for the effects of a number of different radiation sources and the variation in different viewing angles, it is conceivable that there will be discrepancies. Nevertheless, the daytime flight comparison results are reasonably good considering the ±1.0℃ measurement uncertainty of the thermal camera. For the nighttime flight comparison results, there seems to be systematic biases against measurement of low object temperature (a few degrees lower than i-button temperature measurements), likely due to the assumption in the calculation of atmospheric transmittance.

4. Development of automatic micro-climate stations

4.1 Requirements for the micro-climate stations

To study urban micro-climate, the existing network of i-button sensors can only operate passively and take measurements of air temperature once every 5 minutes in order to extend their operation time due to limited battery life. This is apparently not desirable. Prototypes of fully automatic multi-sensor micro-climate stations have been developed by the Observatory with a view to providing real-time weather data and increasing the number of weather elements gathered at each observation site for micro-climate studies.

In developing these prototypes, several design and fabrication criteria have to be considered:

(1) Sensor uncertainty;
(2) Control interface and system integration;
(3) Size and appearance of the micro-climate station;
(4) Power consumption; and
(5) Method of data transmission.

Most often, the site for installation of a micro-climate station usually has more limitations than that of a conventional automatic weather station, for example lack of open space, unavailability of power supply or suitable communication link, etc. Besides, the appearance of the micro-climate station should be designed in a way to integrate well with its surroundings.

Nowadays, increasing varieties of MEMS sensors are available on the market with reasonable uncertainty and affordable prices. In the development of the Observatory's prototype micro-climate stations, MEMS sensors have been chosen to measure temperature, relative humidity, air pressure, and UV-index. Typical factory declared uncertainties of these MEMS sensors are within ±0.5°C, ±5%RH, ±1hPa, and ±0.5UVI for the respective elements mentioned above. Figure 10 shows an example of an external, exchangeable module of a micro-climate station with MEMS sensors to measure temperature and humidity. An added benefit from using MEMS sensors is that they can also be interfaced with small microprocessor units through the I^2C serial communication protocol, which is advantageous when small footprint multiprocessors with limited peripheral output lines are used to control measurements from multiple sensors.

3-D printing technology has also opened the capability to develop and fabricate accessories for the multi-sensor modules during the development of the prototype micro-climate stations. Figure 11 shows various designs of the radiation shields and housings for the electronics of the micro-climate stations using 3-D printing technology.

4.2 Prototype Micro-climate Stations

Two prototype micro-climate stations have been established by the Observatory, one at Zero Carbon Building (ZCB) in East Kowloon and another at the Observatory's Headquarters (HKO) (see Figures 12 and 13 respectively). These two stations serve as good testbeds to test the design and operation of the in-house built micro-climate stations through which further enhancements can be made.

For the micro-climate station at ZCB (Figure 12), six measurement nodes with multiple weather sensors have been installed at different locations of the site, measuring the micro-climate at those locations. The two measurement nodes A and D are mounted on lampposts with the sensors installed at about 2m above ground. These measurement nodes are installed with sensors to measure air temperature, relative humidity, air pressure, and an ultrasonic anemometer to measure wind speed and direction (see a sample photo in Figure 14 (a) and (b)). Two other measurement nodes B and E, designed as garden lighting bollards (see a sample photo in Figure 15) are installed with sensors to measure temperature and RH sensors at about 1 m above ground and at the edge of paved walkways. The measurement node B also has a sensor to measure the UV Index. A third bollard type measurement node at F is installed with sensors to measure temperature and RH underneath the cover of a tree. To measure the heat stress at ZCB, a WBGT Heat Stress Monitoring System has also been installed at location C. Micro-climate at the site should then be available for analysis through data gathered by this network of measurement nodes.

In respect of the micro-climate station at HKO (Figure 13), three prototype measurement nodes, two bollard types and one specifically for mounting on a lamppost, have been developed. Figures 14 and 15 show the measurement nodes at the lamppost and bollard respectively. Through the establishment of these measurement nodes, comparison with weather elements measured near the vicinity of the site has been made and enhancement is being made to improve the radiation shields and the robustness of measurement.

4.3 Method of Data Transmission

Within a local micro-climate station network like the ones at ZCB and HKO, each multi-sensor micro-climate measurement node would transmit its data through low-powered radio frequency RF link to a designated local gateway, which in turn relays the data to a database server in the cloud via mobile GPRS connectivity. With this configuration, data collection from a number of micro-climate measurement nodes can be coordinated by a single local gateway and also keeps the use of high power consuming GPRS modem to one per local gateway rather than one for each multi-sensor measurement node (Figure 16).

However, the use of GPRS modems can only be applicable to locations that either have access to external DC/AC power or have sufficient space and exposure for installing larger solar panels to provide enough power for the operation of the gateways. Among other data transmission pathways, LoRaWAN, a Low Power Wide Area Network (LPWAN), an emerging and widely accepted international standard has also been chosen by HKO for the implementation of micro-climate station network due to its low power consumption and long range. Four LoRaWAN gateways, three from HKO and one from a local university, have already been installed (Figure 17). The three gateways set up by HKO can essentially cover most of the i-button temperature measurement sites described in Section 2 (Figure 18). It is also planned that more such gateways will be installed in the years to come to better support the micro-climate study in Hong Kong.

5. Discussion

The occurrence of hot spell in the period of 17 May – 1 June 2018 demonstrated again the generally reversed pattern of heat distribution over the Kowloon peninsula under the easterly and westerly wind regimes. As more wind sensors would be installed at the micro-climate stations, further detailed assessment of the ventilation conditions over the Kowloon peninsula under different meteorological scenarios can be carried out in addition to utilizing Computational Fluid Dynamic (CFD) models to perform the analysis.

The high resolution thermal maps provide useful information on the heat characteristics of different land surfaces which are useful for assessing the urban heat island effect and for urban planning. The comparison results as mentioned in Section 3 suggest that emissivity-derived surface temperatures were, in terms of order of magnitude, a good approximation to the estimation of surface temperatures of different land surfaces. For the systematic negative bias of the emissivity-derived surface temperatures based on the

nighttime flight data on 14 January 2018, it was thought that the presence of a weak inversion near the height of 300m - 400m (Figure 9) might have affected the derivation as it was assumed that the vertical distribution of both temperature and relative humidity would be uniform between the ground and the helicopter flight level. More flight data would be required for verifying this hypothesis.

Besides, the i-button sensors network has a great potential to be enhanced due to its dense distribution over urban areas. Various aspects including data communication, fabrication methods, and mounting method were explored. The ideas suggested that the newly developing weather monitoring sensors are able to be integrated in urban structures such as lampposts. The gathered real-time weather data could be analyzed to facilitate smart city planning.

6. Conclusion

This paper presents the results so far obtained from the passive i-button temperature sensors. During a 16-day heat wave period in 2018, the two days with a reverse change of wind direction over the Kowloon peninsula were studied. In the first day, it was found that the temperatures over the western flank of the region near the sea side were around 2 degrees lower than that of the eastern flank under west to southwesterlies. On the next day, the situation reversed under easterlies conditions, consistent with the earlier findings in Chan and Fan (2017).

Steps and thoughts in developing a network of micro-climate stations providing real-time weather data for use in urban climate studies are also highlighted. LoRaWAN is expected to provide a lower power option for real-time data transmission. With the gradual enhancement of a dense weather monitoring network, a variety of potential applications for smart city planning is anticipated.

7. Acknowledgment

The authors would like to thank Miss K. Y. Cheng for designing various types of radiation shields. The authors would also like to thank Mr K. C. Tsui and Mr K. H. Tam for their invaluable advice and comments. Special gratitude is also given to the Department of Land Surveying and Geo-Informatics of the Hong Kong Polytechnic University and the Government Flying Service of Hong Kong for their invaluable support in provision of the thermal camera and operating the helicopter flights respectively for this study.

8. References

Chan, Y.W. and M.H. Fan (2017). Application of button-size temperature sensors for micro-climate study of the urban environment of Hong Kong. Paper presented at the WMO International Conference on Automatic Weather Stations, Offenbach am Main, Germany, 24-26 October 2017.

Hong Kong Observatory (2018). Monthly Weather Summary (available at: http://www.hko.gov.hk/wxinfo/pastwx/mws2018/mws201805.htm).

Huang, Weijiao, Jun Li, Qiaoying Guo, Lamin R. Mansaray, Xinxing Li and Jingfeng Huang (2017). A Satellite-Derived Climatological Analysis of Urban Heat Island over Shanghai during 2000–2013. Remote Sens. 9, 641, 2017.

Kaplan, Gordana, Ugur avdan and Zehra Yigit Avdan (2018). Urban Heat Island Analysis Using the Landsat 8 Satellite Data: A Case Study in Skopje, Macedonia. Presented at the 2nd International Conference on Remote Sensing, 22 March – 5 April 2018 (available at: https://sciforum.net/conference/ecrs-2).

Peng, Fen, M.S. Wong, C.H. Ho, Janet Nichol and PW Chan (2017). Reconstruction of historical datasets for analyzing spatiotemporal influence of built environment on urban microclimates across a compact city. Building and Environment (available at: http://www.sciencedirect.com/science/article/pii/S0360132317303372?via%3Dihub).

Tam, K.H., K.W. Chan and Y.W. Chan (2017). Advancement of Community Weather Information Network through the use of Low-cost Automatic Weather Station. Paper presented at the WMO International Conference on Automatic Weather Stations, Offenbach am Main, Germany, 24-26 October 2017.

Table 1 **Comparison of surface temperatures derived from ortho-rectified thermal maps (taken during daytime flight (top) and nighttime flight (bottom) on 14 January 2018) and temperature measurements of i-button sensors placed on the surfaces.**

Daytime flight from 13:32 to 14:43 on 14 January 2018					
Station	*Surface*	**(A)** *Surface Temperature derived from Thermal Map (^oC)*	**(B)** *Surface Temperature measured by i-button sensor during flight time (^oC)*	**(A)** lies within range of **(B)** ?	If No, smallest difference between **(A) and (B)** *(^oC)*
HKO	Grass	16.9	16.1 - 17.4	Yes	-
	Concrete	30.7	30.5 - 32.2		-
A2	Grass	28.2	27.7 - 32.1		-
A3	Grass	28.0	26.3 - 28.9		-
KP	Grass	31.5	32.0 - 34.9	No	-0.5
	Concrete	33.1	30.6 - 33.4	Yes	-
T13	Grass	33.1	33.8 - 35.7	No	-0.7
T26	Grass	23.2	21.2 - 23.6	Yes	-
Nighttime flight from 20:30 to 21:35 on 14 January 2018					
Station	*Surface*	**(A)** *Surface Temperature derived from Thermal Map (^oC)*	**(B)** *Surface Temperature measured by i-button sensor during flight time (^oC)*	**(A)** lies within range of **(B)** ?	If No, smallest difference between **(A) and (B)** *(^oC)*
HKO	Grass	10.2	13.1 - 13.2	No	-2.9
	Concrete	13.0	14.5 - 14.9		-1.5
A2	Grass	11.5	13.9 - 14.3		-2.4
A3	Grass	9.6	12.4 - 12.7		-2.8
KP	Grass	8.3	12.0 - 12.5		-3.7
	Concrete	13.1	16.2 - 16.9		-3.1
T13	Grass	9.6	12.0 - 12.6		-2.4
T26	Grass	9.0	12.3 - 12.5		-3.3

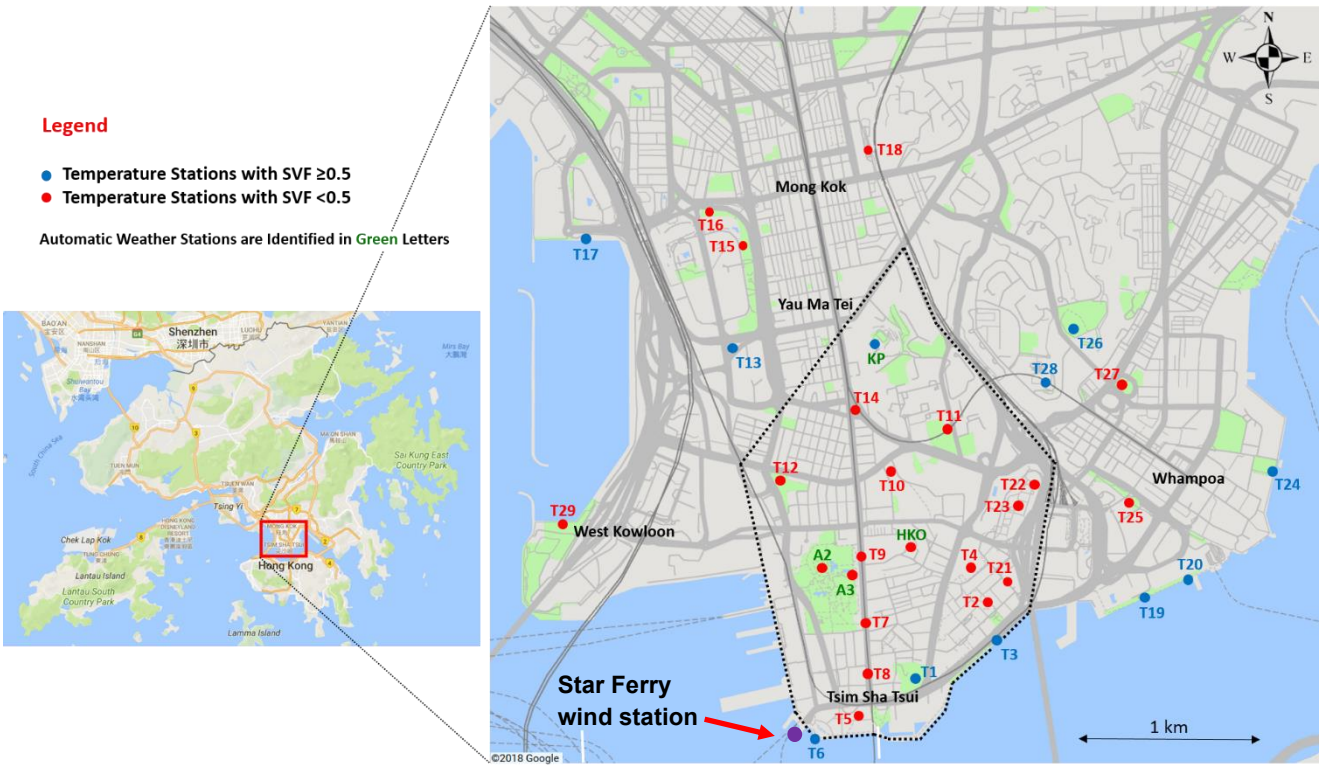

Figure 1 I-button temperature observation network over the Kowloon peninula. Sites with good exposure (sky view factor, SVF > 0.5) are shown in blue dots. Sites with SVF ≤ 0.5 are shown in red dots. HKO and KP represent stations at Hong Kong Observatory Headquarters and King's Park Meteorological Station respectively.

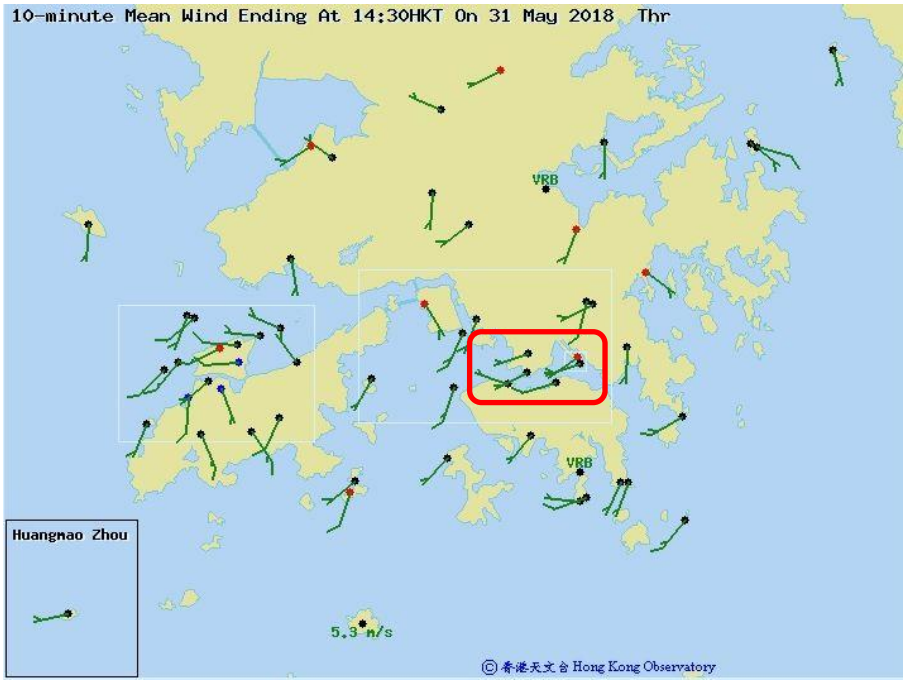

Figure 2 The wind flow conditions over Hong Kong at 2:30 p.m. on 31 May 2018 with west to southwesterlies generally prevailing over the Kowloon peninsula (red rectangle).

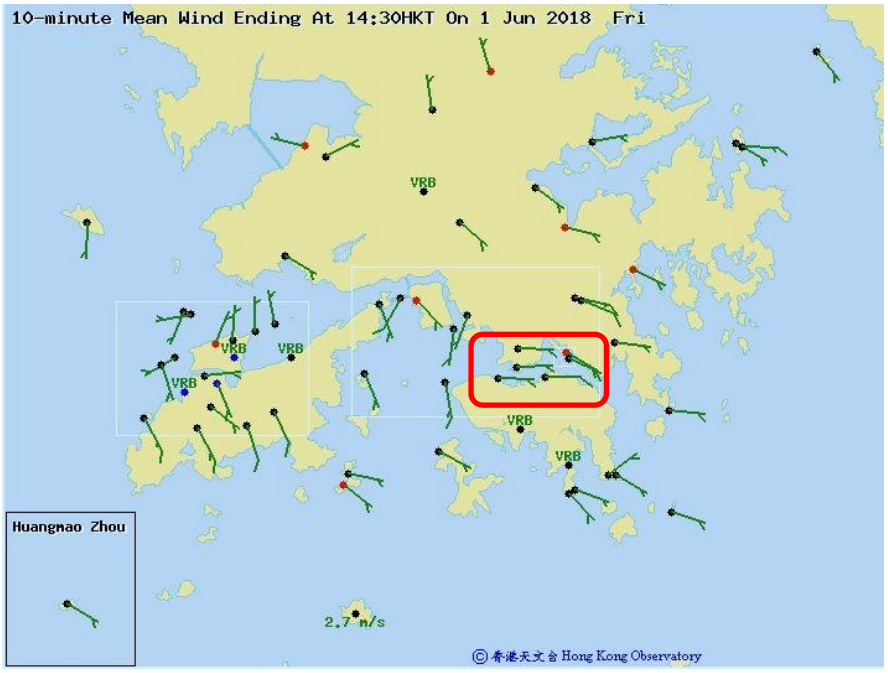

Figure 3 The wind flow conditions over Hong Kong at 2:30 p.m. on 1 June 2018 with easterlies generally prevailing over the Kowloon peninsula (red rectangle).

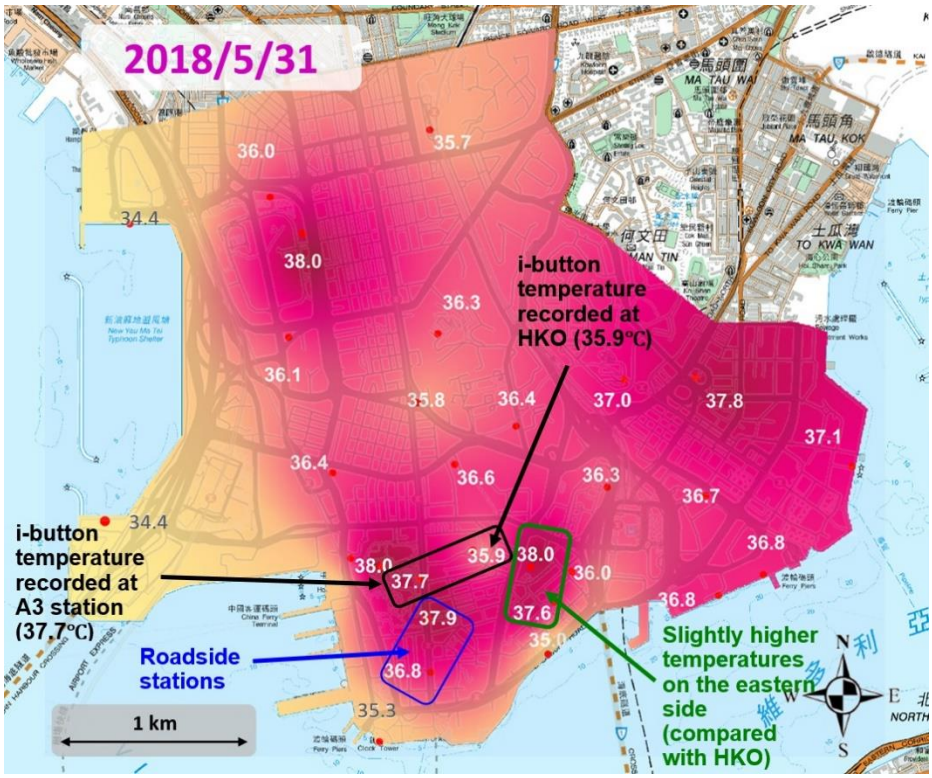

Figure 4 Temperature distribution over the Kowloon peninsula at 2:30 p.m. on 31 May 2018.

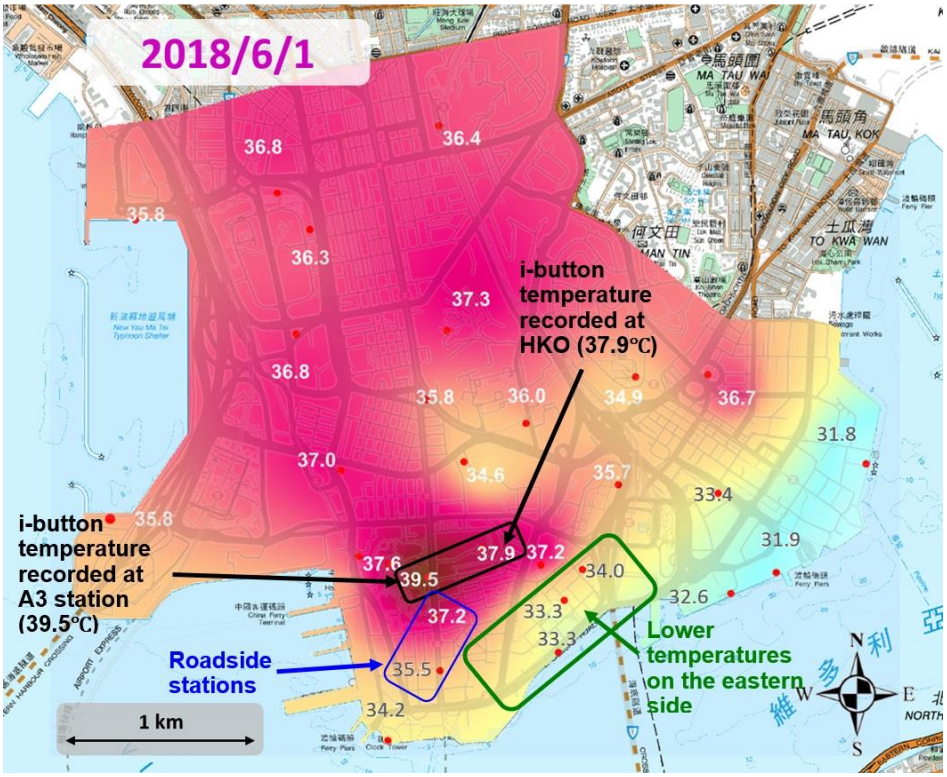

Figure 5 Temperature distribution over the Kowloon peninsula at 2:30 p.m. on 1 June 2018.

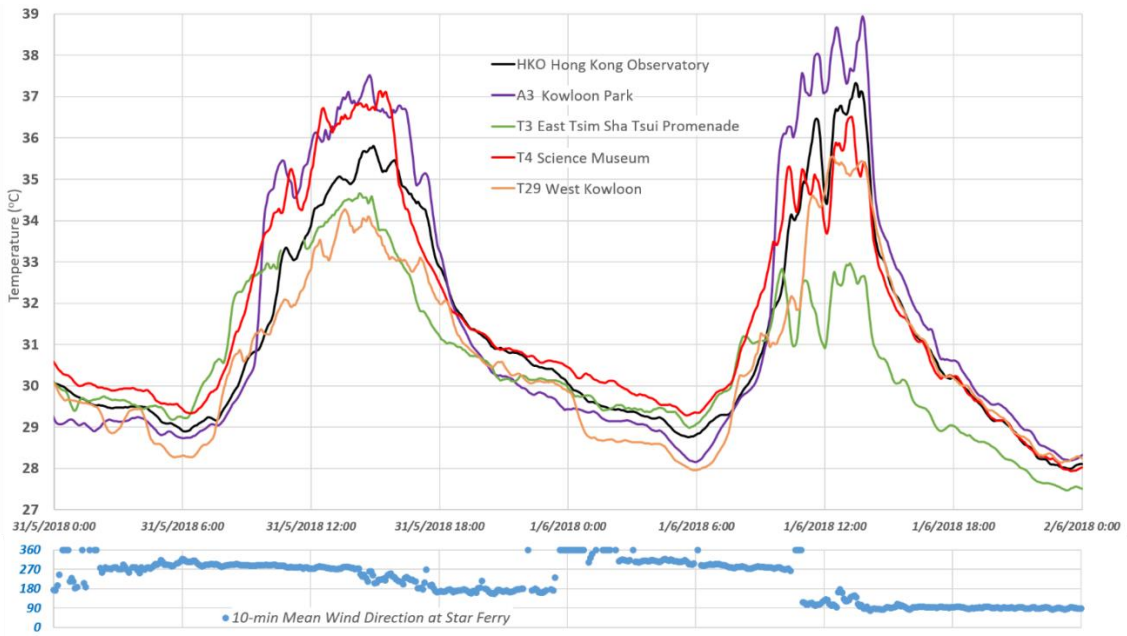

Figure 6 Time series of temperatures recorded at HKO, A3, T3, T4 and T29 stations on 31 May and 1 June 2018 (upper panel). Times series of wind direction recorded at the Star Ferry wind station on 31 May and 1 June 2018 (lower panel).

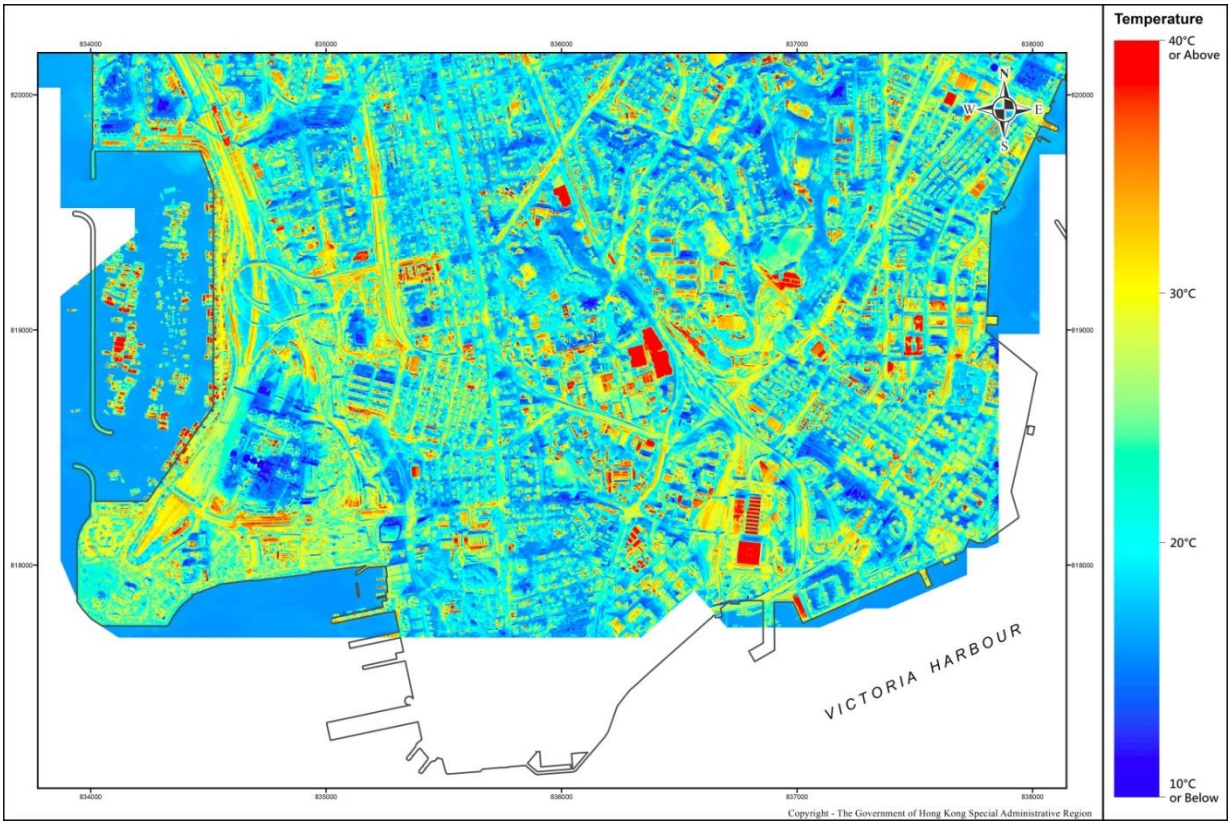

Figure 7 Ortho-rectificed thermal maps on 14 January 2018 (Daytime).

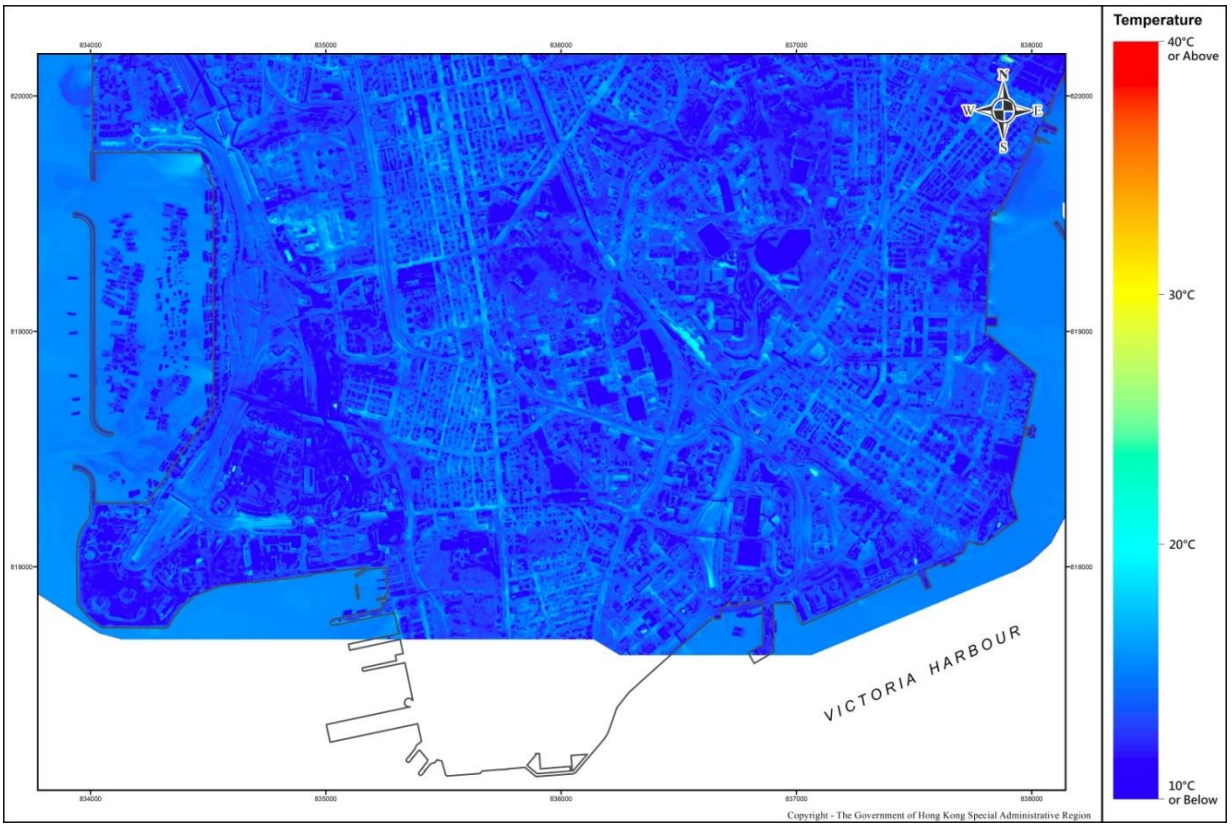

Figure 8 Ortho-rectificed thermal maps on 14 January 2018 (Nighttime).

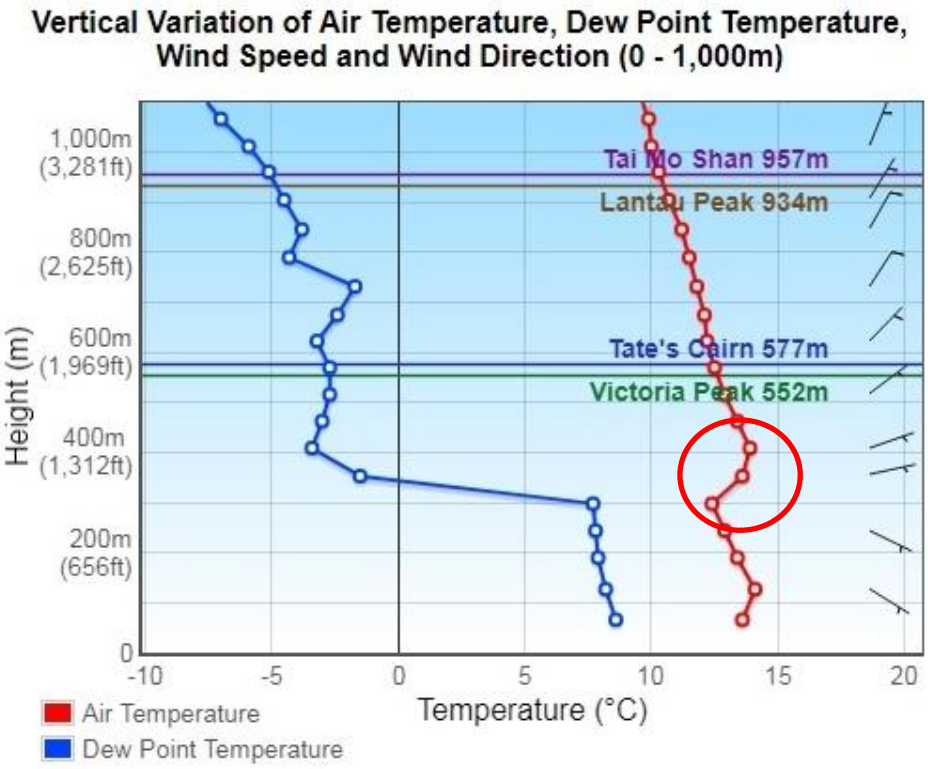

Figure 9 Vertical variation of air temperature, dew point temperature and winds in the lower atmosphere (–up to around 1,000m in height) on the night (8 p.m.) of 14 January 2018 with the red circle showing a weak inversion near 300m - 400m.

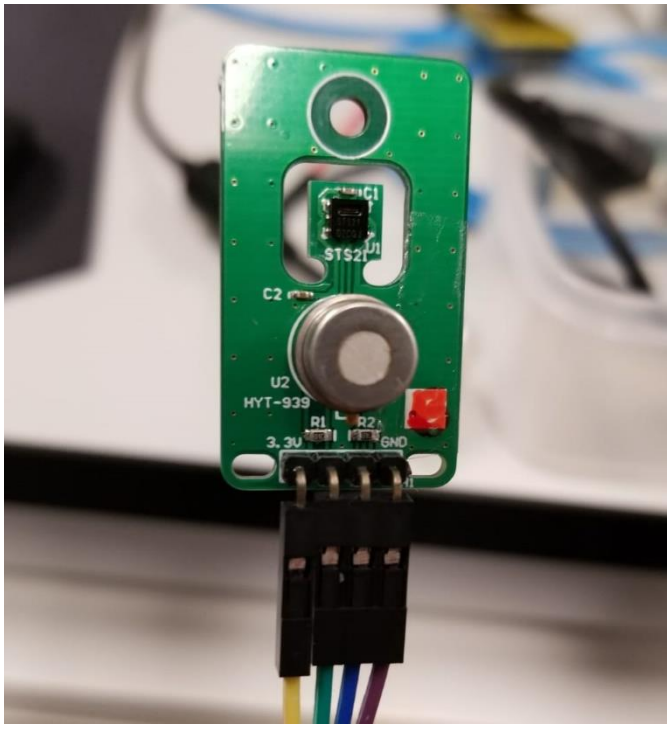

Figure 10 Prototype of an external, exchangeable module of a micro-climate station with MEMS sensors to measure temperature and humidity.

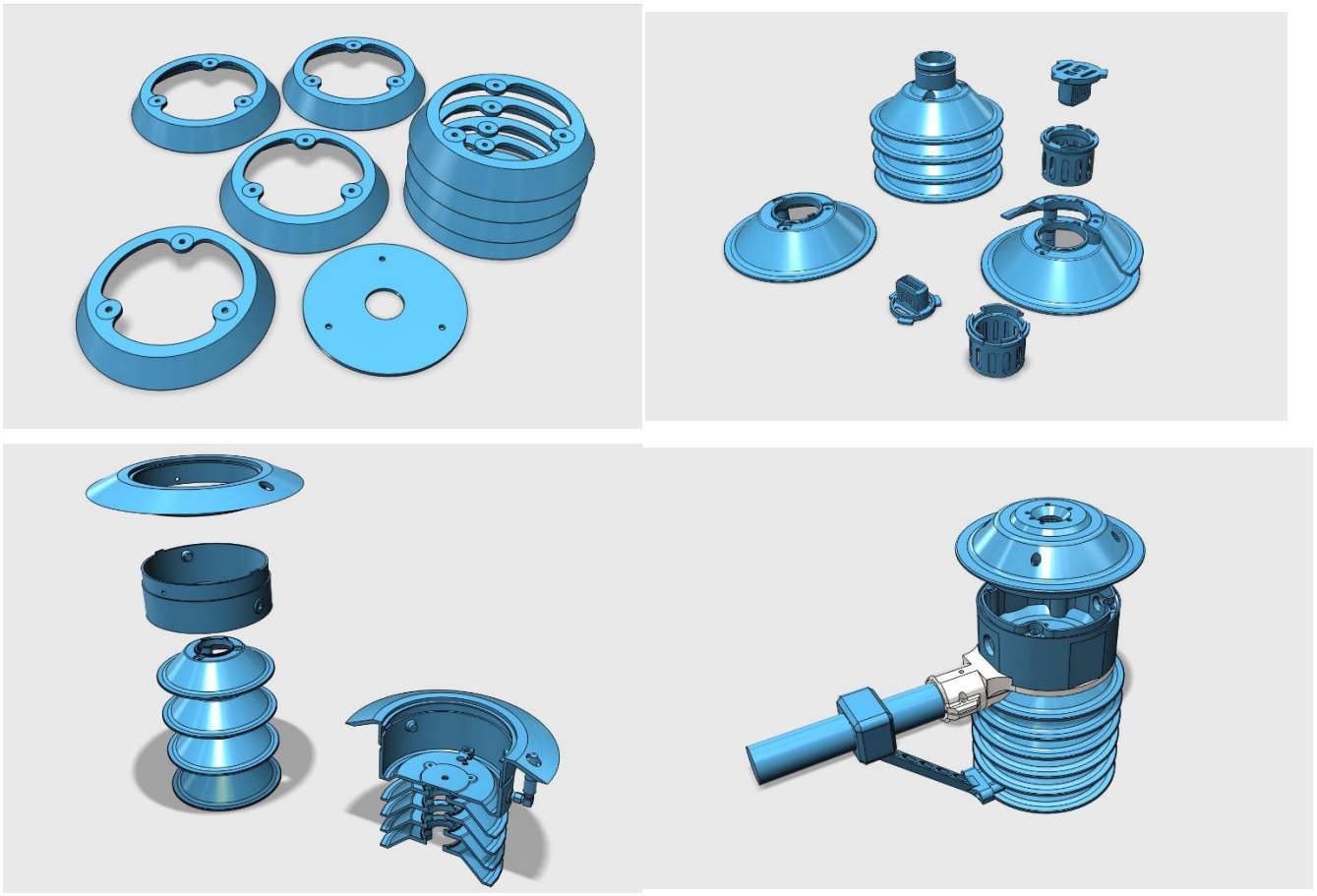

Figure 11 Illustration of the various designs of the radiation shields and housings for the electronics of the micro-climate stations using 3-D printing technology.

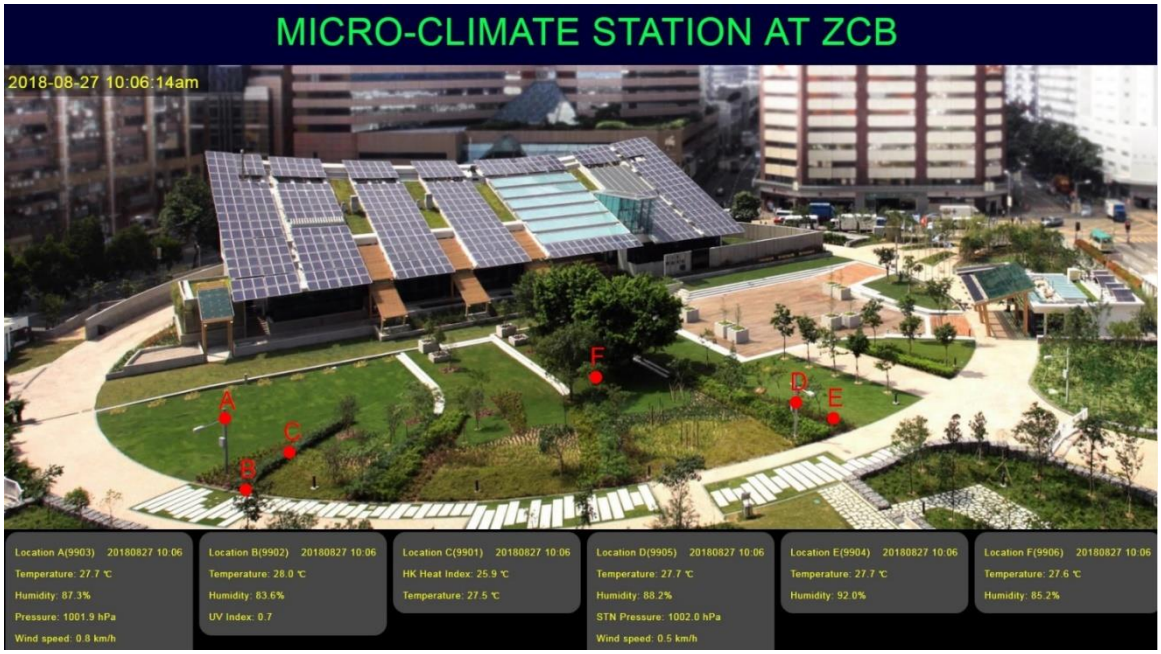

Figure 12 Locations of the measurement nodes and their respective measured weather elements at the micro-climate station at Zero Carbon Building in East Kowloon.

Figure 13 Locations of the measurement nodes and their respective measured weather elements at the micro-climate station at HKO Headquarters.

(a) (b)

Figure 14 The prototype micro-climate measurement node mounted on a lamppost at HKO Headquarters (a). A close-up of the measurement node is shown in (b). The black cylinder-like object at the top is the ultrasonic anemometer. The white enclosure and radiation shield are made using 3-D printing technology.

Figure 15 The solar-powered bollard type micro-climate measurement node at HKO Headquarters. Temperature, RH as well as UV Index are measured using this bollard. The small black disc at the top left hand side of the bollard is the UVI detector.

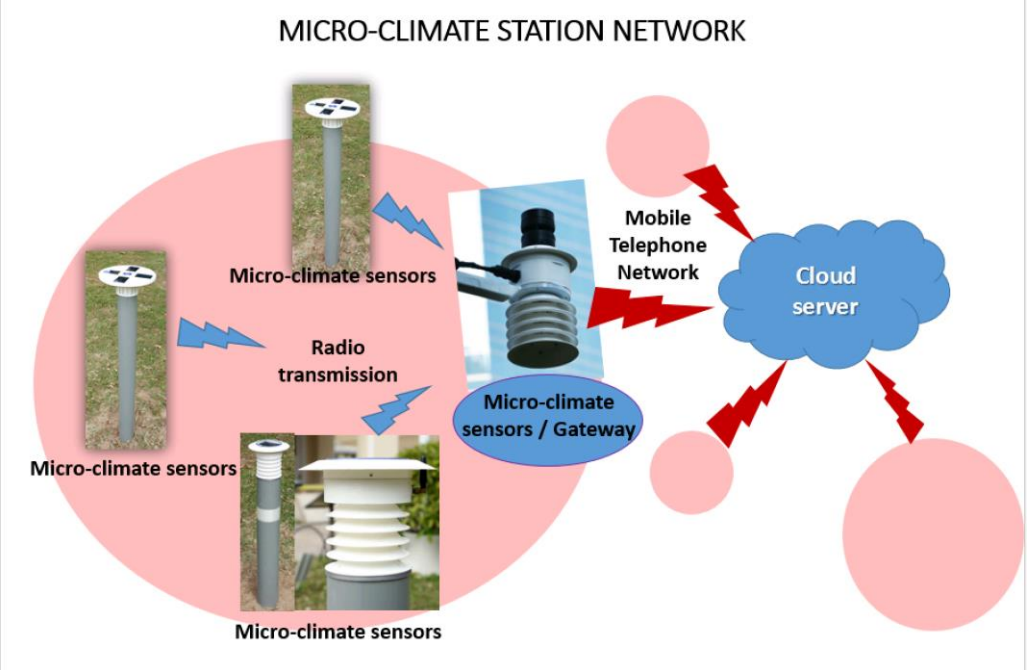

Figure 16 Data transmission path of a typical micro-climate station network of the Observatory.

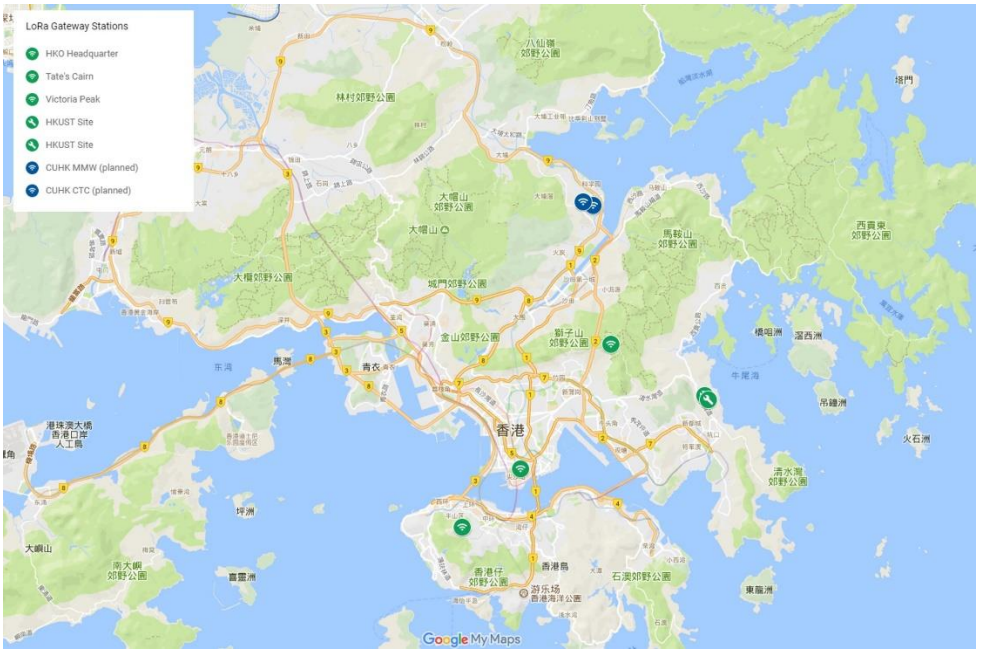

Figure 17 The LoRaWAN being set up by the Observatory. Labels in green show the LoRa gateways that have already been built while those in blue are planned ones.

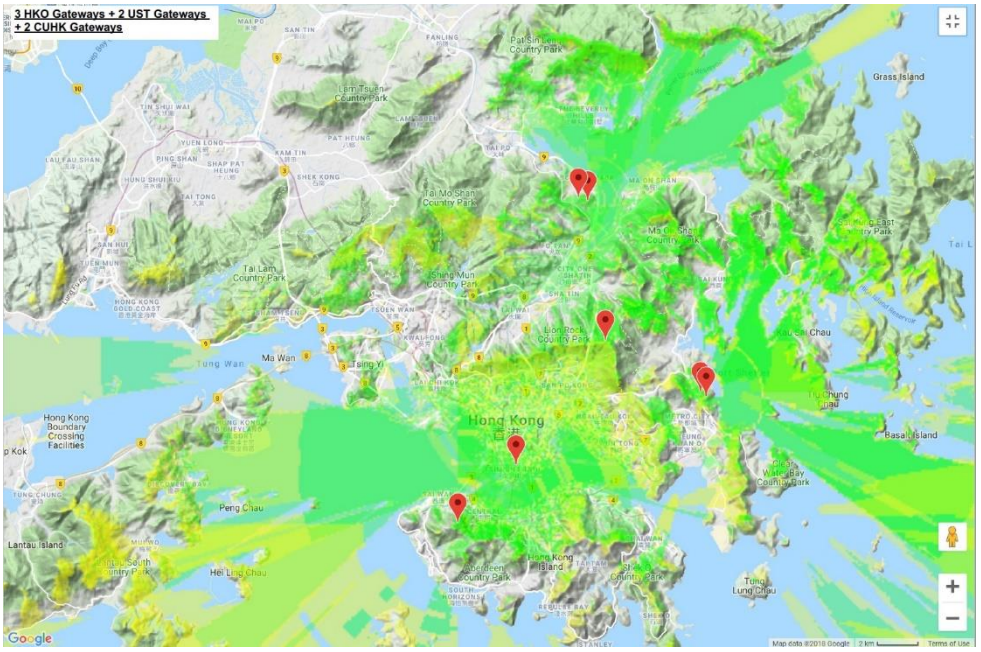

Figure 18 Simulated coverage of the LoRaWAN based on gateways in Figure 17.